Research Article

Comprehensive study of α-MgAgSb: Microstructure, carrier transport properties, and thermoelectric performance under ball milling techniques

Song Yi Back[a,1,*], Steph Meikle[a,b,1], Takao Mori[a,c,*]

[a]Research Center for Materials Nanoarchitectonics (MANA), National Institute for Materials Science (NIMS), Namiki 1-1, Tsukuba 305-0044, Ibaraki, Japan

[b]Materials Science and Engineering Department, University of Florida, Gainesville, Florida 32611, United States

[c]Graduate School of Pure and Applied Sciences, University of Tsukuba, Tennodai 1-1-1, Tsukuba 305-8671, Ibaraki, Japan

[1] These authors contributed equally to this work.

*Corresponding authors.

E-mail addresses: BACK.Songyi@nims.go.jp (Song Yi Back), MORI.Takao@nims.go.jp (Takao Mori).

Abstract

This study investigates the crystal structure, microstructure, electronic, thermal transport properties, and thermoelectric performance of α-MgAgSb synthesized through various ball milling techniques. Variations in synthesis methods can significantly impact thermoelectric performance. Our findings indicate that impurity phases, particularly the secondary phase Ag_3Sb, hinder grain growth and decrease carrier mobility. By systematically adjusting milling conditions, the increased grain size resulting from the suppression of impurity formation improves charge carrier mobility and enhances the power factor. Low-temperature resistivity analysis reveals distinct scattering mechanisms influenced by impurity levels. α-MgAgSb with a tiny content of Sb primarily exhibits electron-electron scattering, whereas higher impurity levels introduce both electron-electron and electron-phonon scattering. Additionally, thermal conductivity analysis using three Effective Medium Theory (EMT) methods shows that the distribution of Ag_3Sb increases interfacial resistance. The maximum zT value of 1.36 was achieved in a compound with an α-MgAgSb to Sb ratio of 99%:1%.

Keywords: α-MgAgSb, Thermoelectrics, Ball milling, Carrier transport, Microstructure

1. Introduction

Waste heat is commonly dissipated into the environment due to industrial, commercial, and automotive processes, which poses questions of concern related to global warming and energy efficiency issues. As an effort to mitigate waste heat loss, investigation, and development of thermoelectric (TE) materials is meaningful. TE materials, exhibiting semiconductor behavior, can compose solid-state devices that convert heat into electric power, and vice versa [1–4]. The dimensionless figure of merit (zT), zT $= S^2\sigma T/(\kappa_\mathrm{l} + \kappa_\mathrm{e})$, where S, σ, T, κ_l and κ_e are the Seebeck coefficient, electrical conductivity, absolute temperature, lattice thermal conductivity and electronic thermal conductivity, characterizes the thermoelectric performance of a material. A trade-off between the temperature-dependent S, σ, and κ_e exists to achieve high performance, prompting a multifaceted investigation of the effects of synthesis modification on TE properties. For instance, enhancing $S^2\sigma$, otherwise known as the power factor (PF), while suppressing lattice thermal conductivity κ_l is imperative for maintaining a high zT [5–9]. Furthermore, total thermal conductivity of a thermoelectric material is the sum of the electronic and lattice thermal conductivity, as given by $\kappa = \kappa_\mathrm{l} + \kappa_\mathrm{e}$. With regard to suppressing κ_l, both the electronic thermal conductivity and the electrical conductivity are proportional to the charge carrier concentration, which establishes a trade-off between PF and κ_e. This explains why efforts are underway to suppress κ_l. Advancements focus on optimizing thermoelectric properties have focused on optimizing properties through band structure engineering [10–15] and nanostructuring [5,6,16–18], aiming to enhance thermoelectric performance.

α-MgAgSb has emerged as a promising thermoelectric material due to its unique properties and potential applications for mid-temperature from 300 K to 550 K, which can replace traditional thermoelectric material Bi_2Te_3 [19–23]. MgAgSb exhibits three distinct phases characterized by structural and electronic properties at different temperature ranges [24,25]. The α-phase (space group $I\bar{4}c2$) behaves as a typical p-type semiconductor at low temperatures (below 573 K). In the temperature range of 573–643 K, the β-phase (space group $P4/nmm$) displays metallic properties. Above 643 K, the γ-phase (space group $F\bar{4}3m$) adopts a half-Heusler structure and exhibits semiconducting behavior. Among these, the α-phase MgAgSb is particularly notable for its low thermal conductivity, which is attributed to significant local disorder within the crystal lattice [26–29]. This intrinsic disorder scatters phonons effectively, reducing thermal conductivity, which enhances the thermoelectric performance.

Its potential to replace traditional Bi-Te-based materials is particularly significant, given the abundance and lower cost of its constituent elements. The n-type Mg_3Sb_2-based compounds are widely studied as counterparts to the p-type semiconducting α-MgAgSb [30–38]. While both materials achieve high thermoelectric performance, α-MgAgSb exhibits lower performance compared to Mg_3Sb_2-based materials.

Numerous studies have focused on developing high-performance α-MgAgSb. Various approaches, such as band engineering [39], doping (Li [29], In [40], Zn [41–43], and Yb [44]), and defects [45,45], have been explored to enhance thermoelectric performance. Notably, obtaining a pure phase of α-MgAgSb has been challenging, often leading to intrinsic Ag- and Sb-deficiencies and the formation of secondary phases. Therefore, recent research continues to explore synthesis parameters to improve the purity of the MgAgSb phase, including sintering conditions and ball milling techniques [50]. For example, different ball milling techniques can yield distinct impurity compositions within α-MgAgSb, as demonstrated in comparisons between high-energy and planetary ball milling methods [51]. While it is reported that the two-step ball milling process has successfully yielded α-MgAgSb phase without secondary phases [52], implementing a cleaning step during the two-step ball milling process can either reduce impurities further or introduce new impurity phases, underscoring the complexity of synthesis method effects on the properties of α-MgAgSb [47]. Modifying the melting method, for example, by using various quartz tubes such as carbon-coated silica and tantalum-sealed tubes, provides control over the types and levels of impurity phases [40,53]. Microwave-assisted synthesis of α-MgAgSb differs from conventional box furnace melting by including minor quantities of Ag_3Sb [54]. Subsequent annealing for two weeks also enables the achievement of the pure α-MgAgSb phase through a combination of ball milling (BM), spark plasma sintering (SPS), and post-annealing [25]. However, the effectiveness of annealing varies; annealing for one week yielded α-MgAgSb along with secondary phases such as Sb and Ag_3Sb, which could be due to annealing temperature or preceding processing steps [24].

While most previous studies primarily focused on the synthesis process for material design and described the general thermoelectric performance of α-MgAgSb [46–49,51], our research examines in-depth the specific carrier transport mechanisms. We clarify how systematic modifications of BM conditions impact the properties of α-MgAgSb by elucidating how secondary phases influence its structural characteristics, carrier transport behavior, and overall thermoelectric performance.

By methodically modifying BM strategies, we observed a direct correlation between refined grain size distribution and enhanced charge carrier mobility, leading to an improved power factor. Low-temperature electrical resistivity analysis below the Debye temperature revealed that in α-MgAgSb with negligible levels of secondary phase Sb, electron-electron scattering dominates carrier transport. In contrast, higher impurity levels introduce both electron-electron and additional electron-phonon scattering, which reduces carrier mobility. This distinction in scattering mechanisms based on impurity levels deepens the understanding of fundamental electronic interactions within α-MgAgSb.

Furthermore, thermal conductivity analysis, conducted using the Effective Medium Theory (EMT), demonstrated that the distribution of Ag_3Sb significantly increases interfacial thermal resistance. Our comprehensive analysis of the microstructural changes induced by different synthesis methods provides an important understanding of how microstructure influences electrical resistivity, carrier mobility, and thermoelectric performance. Ultimately, thermoelectric performance is enhanced by optimizing microstructure and our findings emphasize the critical role of achieving high carrier mobility for high thermoelectric performance of α-MgAgSb.

2. Material and methods

2.1 Synthesis

The α-MgAgSb alloys were prepared by one-step and two-step high-energy ball-milling (BM), with a nominal composition is $MgAg_{0.97}Sb_{0.99}$. In one-step BM process, high-purity Mg (99.95%), Ag (99.99%), and Sb (99.999%) were precisely weighed and loaded into a stainless-steel ball milling jar under an argon atmosphere. Milling was conducted using a SPEX SamplePrep 8000D Mixer/Mill. It has been shown that samples with the stoichiometric composition $Mg_1Ag_1Sb_1$ tend to exhibit Ag- and Sb-related impurity phases [24,43,52,53], and pure single-phase region for MgAgSb in the Mg-Ag-Sb phase diagram is slightly shifted towards the Mg-rich and Sb-rich side [47]. To avoid the formation of impurities, we chose the nominal composition $MgAg_{0.97}Sb_{0.99}$ in our study. The summary of sample identities and synthesis procedures for the prepared samples is provided in Table 1. Samples were labeled as follows: S1 was milled for 5 h, and S2 was milled for 10 h. For the two-step ball-milling method, Mg and Ag were initially processed, followed by the addition of Sb in the second step. S3 was subjected to 5 h of milling in the first step, followed by an additional 10 h in the second step. S4 was subjected to an initial milling period of 10 h, followed by another 10 h in the second step. The ball-milled powders (S1, S2, S3, and S4) were sintered at 573 K for 5 min under a uniaxial pressure of 60 MPa using a Spark Plasma Sintering system (Fuji SPS, DR. SINTER LAB Jr. SERIES 322Lx). Subsequently, sintered samples were annealed in a vacuum quartz tube at 573 K for 6 h. After annealing, the sintered powder was ground in an Ar atmosphere for PXRD measurement, ensuring that the XRD data reflected the structural properties of the as-sintered state. The sintered bulk samples were cut and polished for various other measurements. Ag_3Sb sample was prepared similarly to α-MgAgSb using a one-step ball milling process for 10 h with Ag and Sb, followed by SPS at 573 K under 60 MPa pressure, and post-annealing at 723 K for 24 h.

Table 1 Summary of sample identities and synthesis procedures for MgAgSb samples.

Sample name	One-step BM (h)	Two-step BM (h)
S1	5	-
S2	10	-
S3	5	10
S4	10	10

2.2 Characterization and measurements

Room temperature powder X-ray diffraction (XRD) analysis of samples S1, S2, S3, and S4 was conducted using Cu K_α radiation (40 kV, 15 mA) with a 2θ scan range from 10° to 70° at a scan rate of 1°/min (MiniFlex 600-Cu, Rigaku, Japan). Microstructure analysis was performed using a field emission scanning electron microscope (Hitachi SU8000, Hitachi High-Tech Corporation, Japan) equipped with energy dispersive spectroscopy (EDS) mapping (Xflash Flat QUAD 5060F).

Thermoelectric properties including electrical resistivity $\rho\ (T)$ and Seebeck coefficient $S\ (T)$ above room temperature were measured using a thermoelectric measurement system (ZEM-3, ULVAC-RICO, Japan) under a He atmosphere. Thermal conductivity κ was determined as $\kappa = d_\mathrm{s} C_\mathrm{p} \lambda$, where d_s, C_p, and λ denote sample density (measured using the Archimedes method), heat capacity, and thermal diffusivity, respectively. Thermal diffusivity was measured by the laser flash diffusivity method (LFA-467, Netzsch, Germany).

Electrical resistivity $\rho\ (T)$ at low temperatures (2–300 K) was measured using the PPMS (Physical Property Measurement System, Quantum Design, USA). Hall resistivity ρ_xy measurements were conducted using a four-probe contact method with the PPMS, employing a sweeping magnetic field range of -5 T ≤ H ≤ 5 T. Parameters such as Hall coefficients R_H, Hall carrier concentration n_H, and Hall mobility μ_H were derived from the equations $R_\mathrm{H} = \rho_\mathrm{xy}/H$, $n_\mathrm{H} = 1/eR_\mathrm{H}$, and $\mu_\mathrm{H} = R_\mathrm{H}/\rho = 1/\rho e n_\mathrm{H}$, where the ρ_xy is the Hall resistivity.

Longitudinal (v_l) and transverse (v_t) sound velocities were measured at room temperature using a sing-around ultrasonic velocity measurement instrument (UVM-2, Ultrasonic Engineering Co., Ltd.). The corresponding average sound velocity (v) was calculated via the equation: $v^{-3} = \frac{1}{3}\left(v_\mathrm{l}^{-3} + 2v_\mathrm{t}^{-3}\right)$. Debye temperature is given by $\Theta_\mathrm{D} = \frac{v\hbar}{k_B}\left(\frac{6\pi^2}{V}\right)^{1/3}$.

3. Results and discussion

Fig. 1 depicts the powder X-ray diffraction patterns of samples S1, S2, S3 and S4. The phase quantification analyzed from Rietveld refinement is listed in Table 2. Samples S1 and S2 contain more impurity phases compared to S3 and S4. As the milling time increases, there is a noticeable trend towards higher formation of α-MgAgSb and a decrease in the proportions of secondary phases such as Sb, Ag_3Sb, γ-MgAgSb, and Mg_3Sb_2. The phase ratio of α-MgAgSb increases with increasing ball milling (BM) time as follows: 52% for S1, 81% for S2, 95% for S3, and 99% for S4. The simple one-step BM process was initially applied to examine whether it is feasible to obtain α-MgAgSb with negligible impurities in a time-efficient way. In the case of one-step BM, both S1 and S2 exhibit the main phase α-MgAgSb along with various secondary phases. The Mg_3Sb_2 impurity observed in S1 was effectively eliminated in S2 by increasing the milling time to 10 h. However, S2 still exhibits several impurity phases. The two-step BM approach is employed to further reduce impurities, specifically those related to Sb. Samples S3 and S4 are primarily composed of the α-MgAgSb phase, with S4 showing an exceptionally low proportion of Sb. Sample S3, which was milled for 10 h in the first step followed by 5 h in the second, still contained common impurity phases, such as Ag_3Sb and Sb. In contrast, the highest purity of α-MgAgSb is achieved with sample S4, which involved a total milling duration of 20 h (10 h in each step), emphasizing the importance of the milling process and duration for impurity reduction. This demonstrates that both the number of BM steps and the milling time influence phase composition.

We can estimate the average crystallite size and internal strain of samples by Williamson-Hall plot [55]:

$$\beta\cos\theta = 4\varepsilon\sin\theta + \frac{K\lambda}{D} \tag{1}$$

where β is the full width at half maximum (FWHM) of the diffraction peaks, ε is the internal lattice stain, K (0.9) is the shape factor, λ is the wavelength of the X-ray source, D is the crystallite size, and θ is the peak position in radians. Fig. 1(b) shows the relationship between milling conditions and crystallite size. The average crystallite size of the samples increases monotonically: 60.20 nm for S1, 74.46 nm for S2, 92.30 nm for S3, and 94.64 nm for S4. The internal lattice strain decreases, with values of 0.13 (10^{-4}%), 0.11 (10^{-4}%), 0.13 (10^{-4}%), and 0.09 (10^{-4}%) for samples S1, S2, S3, and S4, respectively, listed in Table S6.

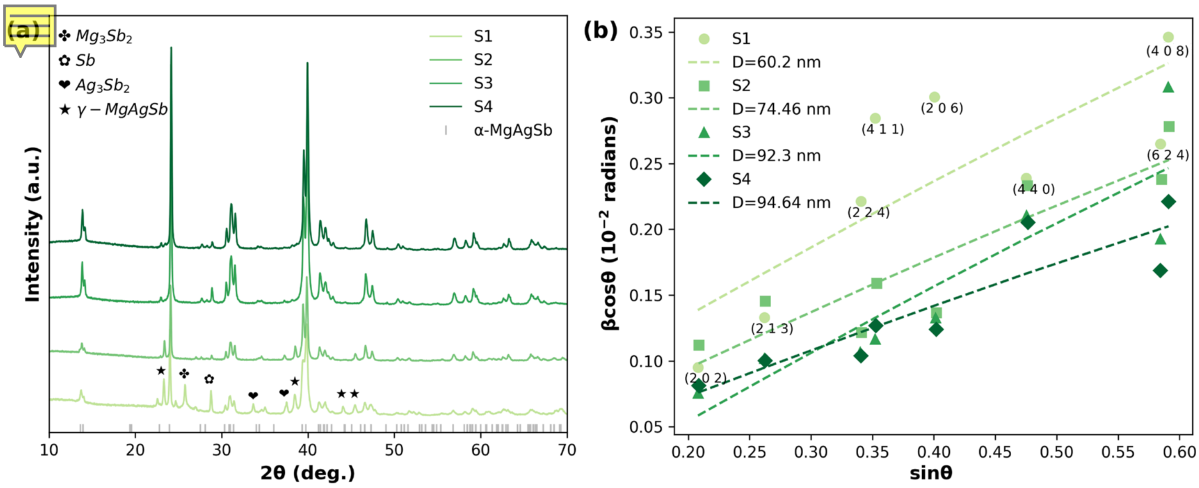

Fig. 1. (a) Powder XRD patterns and (b) Williamson-Hall plot of samples S1, S2, S3, and S4, where *D* is the crystallite size.

Table 2 Phase quantification by using X-ray diffraction analysis and Hall carrier concentration ($\boldsymbol{n}_{\mathbf{H}}$) and mobility ($\boldsymbol{\mu}_{\mathbf{H}}$) for samples S1, S2, S3, and S4.

Sample name	Phase ratio (%)					n_H (10^{19} cm^{-3})	μ_H (cm^2 V^{-1} s^{-1})
	α-MgAgSb	Sb	Ag_3Sb	γ-MgAgSb	Mg_3Sb_2		
S1	52	4	17	10	17	9.46	18
S2	81	1	11	7	0	7.28	29
S3	95	2	3	0	0	4.56	60
S4	99	1	0	0	0	4.60	83

The SEM analysis further complements the XRD results by revealing differences in grain size and impurity distribution. EDS analysis of sample S1 (Fig. 2(a-d)) reveals an inhomogeneous distribution of Mg, Ag, and Sb elements, indicating the presence of Ag_3Sb and Sb within α-MgAgSb. Specifically, Ag_3Sb particles are distributed in sizes ranging from 2–4 µm, while Sb particles are smaller, less than 2 µm (Figs. 2(d) and S3(a)). In contrast, sample S4 exhibits a more homogeneous distribution of elements and larger grain sizes compared to S1, as depicted in Fig. S3. As shown in Fig. 2(e) and (f), the average grain size of samples S1 and S4 are around 9 and 14 µm, respectively. This consistent increase in grain size, which aligns with the crystallite size from XRD, suggests that the BM process not only reduces secondary phases but also promotes grain growth. S1 exhibits multiple secondary phases, including Sb, Ag_3Sb, γ-

MgAgSb, and Mg_3Sb_2, whereas S4 contains a negligible 1% of Sb as a secondary phase. The main phase α-MgAgSb in S4, characterized by considerably low secondary phase content, exhibits superior grain growth compared to S1 with the multi-phase structure. Due to its predominantly single-phase composition with minimal secondary phase content (1% Sb), sample S4 exhibits significantly larger grain sizes compared to S1.

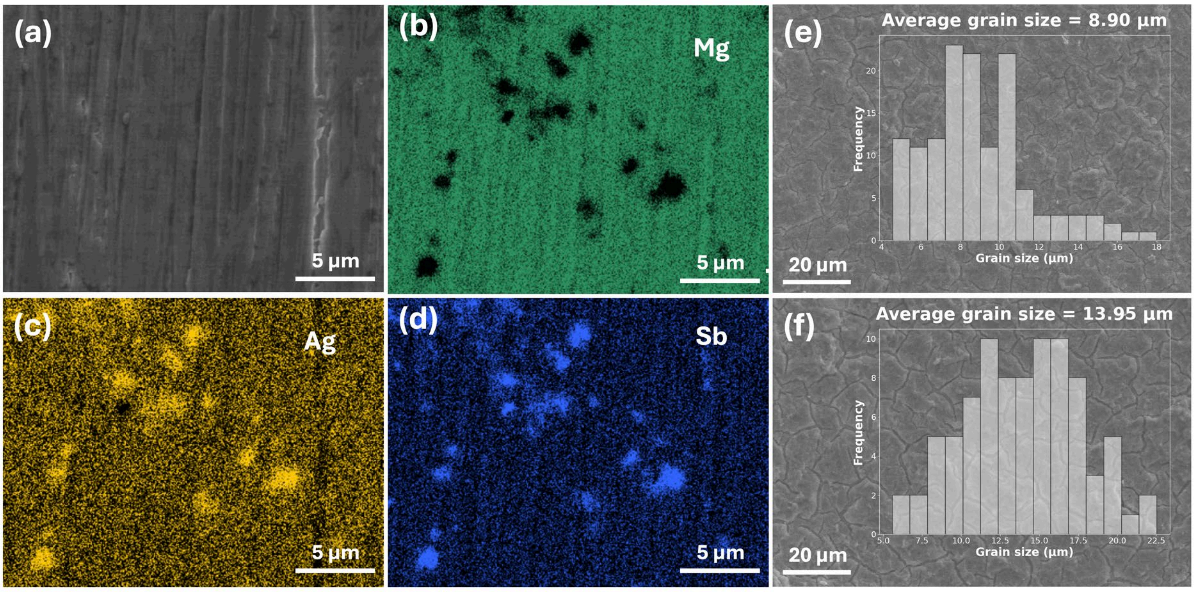

Fig. 2. Microstructural characterizations. (a) SEM and (b-d) EDS mapping images of sample S1. SEM images showing the average grain size of samples (e) S1 and (f) S4.

It is interesting that the grain size increased despite the longer BM duration, which typically would reduce grain size. The potential reasons for this anomaly might be the dissolution of secondary phases and the Zenner pinning effect. As the duration of milling time increases, secondary phases might dissolve back into the matrix MgAgSb, leading to a more homogeneous single-phase material. This can cause grain growth, as the dissolution of secondary phases removes grain boundaries, allowing grains to grow larger.

The different BM processes involve not only the duration but also the sequence of adding Sb into the BM jars. For the one-step BM, all elements—Mg, Ag, and Sb—are milled simultaneously. This increases the high chances of forming impurity phases rather than the α-MgAgSb phase since the area of the α-MgAgSb single phase in a Mg-Ag-Sb phase diagram is small compared to other regions of α-MgAgSb with impurity phases [47]. The formed impurity phases can indeed act as pinning points within the matrix and at the grain boundaries, inhibiting grain growth. In contrast, during the first step of the two-step BM process, only Mg and Ag are involved, forming MgAg. In the second step, Sb is added to the MgAg phase, allowing Sb to dissolve into MgAg and form the α-MgAgSb phase. This two-step BM process provides more chances for the grain growth of the α-MgAgSb phase by preventing the formation of secondary phases.

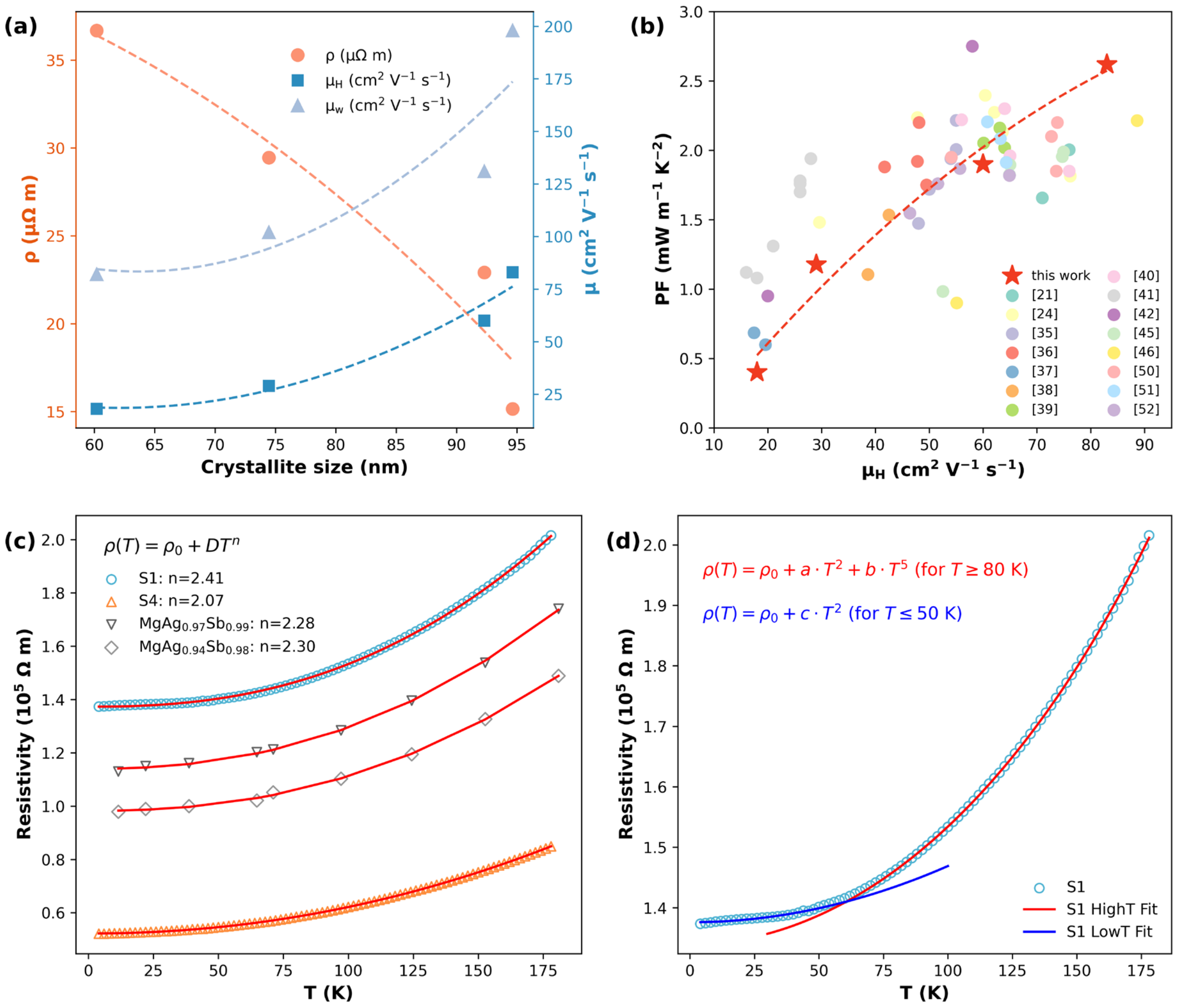

Fig. 3. (a) Electrical resistivity, Hall carrier mobility, and weighted mobility as functions of crystallite size at room temperature. (b) Power factor as a function of Hall carrier mobility at room temperature including this work and literature values [26,29,40–46,49,51,53,56–58]. (c) Temperature-dependent electrical resistivity for samples S1, S4, $MgAg_{0.97}Sb_{0.99}$ [26], and $MgAg_{0.94}Sb_{0.98}$ [26] with experimental data shown as scatter points and fitted results using model 1 represented by a line. (d) Temperature-dependent electrical resistivity for sample S1, with experimental data shown as scatter points and fitted results using model 2 represented by a line.

Fig. 3(a) shows the relationship between electrical resistivity, Hall carrier mobility, and weighted mobility as functions of crystallite size, which was determined using the Williamson-Hall plot at room temperature. The weighed mobility is calculated from the Seebeck coefficient and electrical conductivity using the following equation [59]:

$$\mu_{\mathrm{w}} = \frac{3h^3\sigma}{8\pi e(2m_{\mathrm{e}}k_{\mathrm{B}}T)^{3/2}}\left[\frac{\exp\left[\frac{|S|}{k_{\mathrm{B}}/e}-2\right]}{1+\exp\left[-5\left(\frac{|S|}{k_{\mathrm{B}}/e}-1\right)\right]}+\frac{\frac{3}{\pi^2}\frac{|S|}{k_{\mathrm{B}}/e}}{1+\exp\left[5\left(\frac{|S|}{k_{\mathrm{B}}/e}-1\right)\right]}\right]. \tag{2}$$

As crystallite size increases, there is a marked decrease in electrical resistivity, accompanied by an increase in both Hall mobility and weighted mobility. The grain size of sample S4 is larger than that of S1, as observed in the SEM images (Fig. 2(e) and (f)). Both crystallite size and grain size are linked to the improved quality of the α-MgAgSb phase resulting from the suppression of secondary phase formation. This suggests that the reduction of impurity phases increases the grain size of α-MgAgSb and decreases grain boundary scattering. The smaller grain size in sample S1 leads to a higher density of grain boundaries compared to sample S4, indicating that charge carriers encounter more boundary resistance within the material. Therefore, we conclude that the increase in both crystallite size and grain size, along with the improved quality of the α-MgAgSb phase due to the suppression of secondary phase formation, enhances carrier mobility and reduces electrical resistivity.

Moreover, the decreasing trend of internal lattice strain reflects that the reduction of secondary phases results in the relaxation of internal lattice strain. This reduction in lattice strain is consistent with the increase in mobility, as it can reduce lattice imperfections that scatter charge carriers. Thus, both the grain growth and the relaxation of internal lattice strain contribute to the improved electronic transport properties, reducing resistivity and enhancing mobility.

Fig. 3(b) illustrates the power factor as a function of Hall carrier mobility, incorporating both our experimental results and literature values. The trend clearly indicates that as mobility increases, the power factor exhibits a notable improvement in almost all α-MgAgSb samples. In our samples, the reduction in impurity phases, particularly in sample S4, promotes the dominance of the α-MgAgSb phase and enhances grain growth, which contributes to improved electronic transport properties and improved power factor. Furthermore, the direct interplay between grain size, carrier mobility, and electrical resistivity highlights the critical role of grain size in enhancing the power factor in α-MgAgSb.

For a more detailed analysis of carrier transport properties and thermoelectric performance, we conducted the measurement of electrical resistivity at low temperatures (2–180 K) for samples S1 and S4. Alongside our samples, we extended our investigation to include additional literature samples: $\mathrm{MgAg_{0.97}Sb_{0.99}}$ and $\mathrm{MgAg_{0.94}Sb_{0.98}}$ [26]. Fig. 3(c) depicts the fitting of resistivity for samples S1, S4, $\mathrm{MgAg_{0.97}Sb_{0.99}}$ and $\mathrm{MgAg_{0.94}Sb_{0.98}}$ using the following equation (model 1):

$$\rho\,(T) = \rho_0 + DT^n \tag{3}$$

This equation characterizes the conventional metallic behavior of samples [60]. The residual resistivity, ρ_0, independent of temperature, is proportional to the concentration of the impurity, grain boundaries, defects, and dislocations. The second term represents the temperature dependence of resistivity, where D is a scaling factor and n characterizes the electron scattering mechanism. The large residual resistivity value indicates the abundance of impurities and defects in the material. By eliminating impurity phases, sample S4 exhibits a lower ρ_0 than sample S1 with multiple impurity phases.

As for temperature dependence of resistivity, we found that α-MgAgSb with a larger n-value tends to have lower carrier mobility, as shown in Fig. S4(a). S1 has an n-value of 2.41 with a mobility of 18 cm^2 V^{-1} s^{-1}, whereas S4 has an n-value of 2.07 with a mobility of 83 cm^2 V^{-1} s^{-1}, as shown in Fig. 3(c). The literature samples exhibit the same tendency, including $\mathrm{MgAg_{0.97}Sb_{0.99}}$ with n = 2.28 and a carrier mobility of μ_{H} = 71 cm^2 V^{-1} s^{-1}, and $\mathrm{MgAg_{0.94}Sb_{0.98}}$ with n = 2.30 and μ_{H} = 61 cm^2 V^{-1} s^{-1}. The lower n-value in sample S4 indicates reduced scattering, leading to the improved charge carrier mobility. Consequently, the higher mobility with the low n-value enhances the power factor, as illustrated in Fig. S4(b). Therefore, we propose that the temperature exponent of electrical resistivity at low temperatures can serve as an important indicator of thermoelectric performance.

The quadratic relationship when $n = 2$ indicates that electron-electron scattering dominates across the temperature range below the Debye temperature [60]. The variation in n-value suggests changes in the dominant scattering mechanism. We propose two possible mechanisms to explain the electronic transport behavior in samples S1 and S4, particularly the deviation from the n-value of 2 in sample S1. First, the larger n-value in sample S1 can be interpreted in terms of carrier concentration. A larger n-value indicates that electrical resistivity increases more rapidly with temperature. The high carrier concentration in sample S1, as listed in Table 2, can be related to a lower thermal activation energy, which enhances the thermal excitation of carriers and correlates with a higher n-value due to the increased contribution of scattering from thermally activated carriers and impurities.

Secondly, the larger n-value in sample S1 can also be attributed to enhanced phonon scattering. When the electron-phonon scattering dominates, the electrical resistivity exhibits a strong temperature dependence characterized by the relationship $\rho\ (T) \propto T^5$ according to the Bloch–Grüneisen model [60]. We modeled the resistivity of sample S1 using the following equation (model 2), accounting for both electron-electron and electron-phonon scattering:

$$\rho\ (T) = \rho_0 + aT^2 + bT^5. \tag{4}$$

The fitted resistivity of sample S1 shows two distinct temperature regimes, corresponding to different scattering mechanisms, as shown in Fig. 3(d). At the low temperatures ($T \leq 50$ K), the electrical resistivity fits well to $\rho\ (T) \propto T^2$, indicating that electron-electron scattering dominates. At the high temperatures ($T \geq 80$ K), the exponent increases to 5, reflecting enhanced electron-phonon interactions. This crossover from T^2 to T^5 in sample S1, contrasted with sample S4, which maintains electron-electron scattering dominance throughout the temperature range, suggests that electron-phonon scattering is enhanced due to presence of impurities. Impurities in the material not only influence residual resistivity but also play a significant role in modifying the temperature dependence of resistivity. These impurities introduce defects—such as vacancies, antisite defects, and interstitials—into the lattice, which can alter the density of states near Fermi level. This modification affects both electron-electron and electron-phonon interactions, leading to changes in the dominant scattering mechanisms. As a result, impurities affect not only the residual resistivity but also the temperature exponent of resistivity, as observed in sample S1. In impurity-rich sample S1, the increased n-value can be attributed to the reconstructed Fermi surface, which enhances electron-phonon scattering at higher temperatures. This explains the transition from T^2 to T^5 behavior, reflecting a shift from electron-electron scattering at low temperatures to electron-phonon scattering at higher temperatures.

Fig. 4(a) depicts the electrical resistivity of samples S1, S2, S3, and S4 above room temperature. Fig. S5 demonstrates the repeatability of sample S4, showing heating-cooling data from repeated measurements. The temperature-dependent electrical resistivity above 400 K of samples S1, S1, S3, and S4 are fitted to the following Arrhenius equation [61–63]:

$$\rho(T) = A\exp\left(\Delta/k_\mathrm{B}T\right). \tag{5}$$

This equation is commonly used to analyze typical semiconductor behavior, where Δ is the thermal activation energy. The calculated Δ values are 0.0042, 0.30, 0.26, and 0.28 eV for samples S1, S1, S3, and S4, respectively. The carrier concentration has a relationship with the thermal activation energy, given by $n \propto \exp\left(-\Delta/k_\mathrm{B}T\right)$. Lower thermal activation energy leads to higher carrier concentration at a given temperature. The high carrier concentration promotes the electrically activated states. Sample S1 has a higher carrier concentration due to its lower thermal activation energy than the other samples. This observation is consistent with the electronic transport behavior where we identified the more pronounced temperature dependence of resistivity in sample S1, related to its higher carrier concentration and lower thermal activation energy.

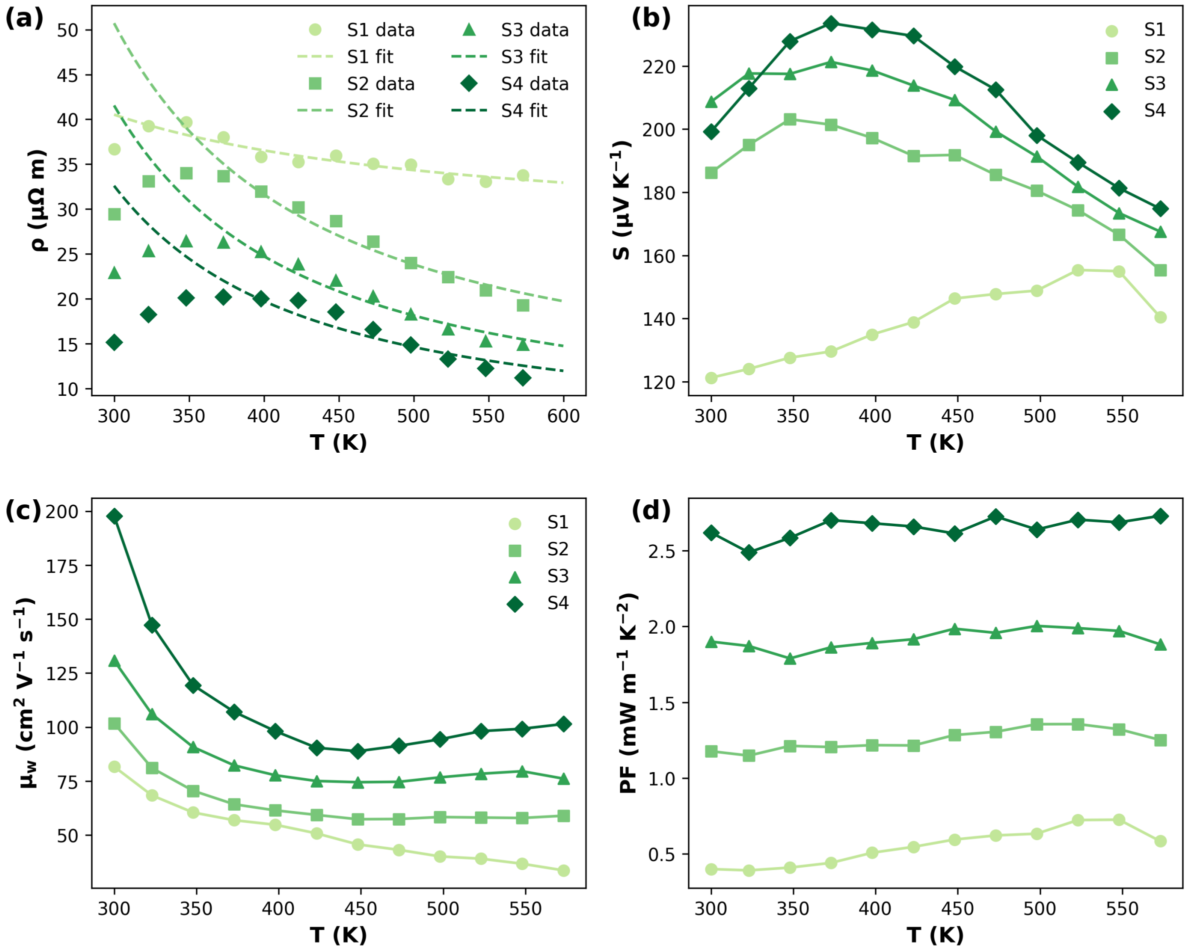

Fig. 4. Temperature-dependent (a) electrical resistivity, (b) Seebeck coefficient, (c) weighted mobility, and (d) power factor of samples S1, S2, S3, and S4.

To model the effect of impurities including the effect of boundary and grain size in transport properties, we assume that our samples consist of two phases: metallic Ag_3Sb and semiconducting α-MgAgSb, and we apply the effective medium theory [64,65], a common approach to describe the transport properties of multi-phase compounds. For the EMT analysis, we utilize the properties of sample S4 as α-MgAgSb and the measured values of Ag_3Sb, which are listed in Table S7. The effective electrical conductivity σ_{eff} is given by:

$$v_1 \frac{\sigma_1-\sigma_{\mathrm{eff}}}{\sigma_1+2\sigma_{\mathrm{eff}}} + v_2 \frac{\sigma_2-\sigma_{\mathrm{eff}}}{\sigma_2+2\sigma_{\mathrm{eff}}} = 0 \quad (6)$$

where σ_1 and σ_2 are the electrical conductivity of phase 1 and phase 2, and v_1 and v_2 are the volume fractions of phase 1 and phase 2, respectively. According to the EMT, the electrical conductivity of samples is expected to be higher as the content of Ag_3Sb increases, as shown in Fig. S6. However, the electrical resistivity of sample S1 with 58% α-MgAgSb, 17% Ag_3Sb, and other impurities are more than double that of sample S4 (37 μΩ·m compared to 15 μΩ·m), which has 99% α-MgAgSb and 1% Sb, not consistent with the simple EMT model.

Kuo et al. proposed a two-phase model composed of a grain phase and a grain boundary phase [66]. This model explicitly accounts for the inhomogeneous nature of the grain boundary region by treating the space-charge region induced by the grain boundary as a separate phase. In this simplified model where the grain and grain boundary phases are connected in a series circuit, the overall electrical resistivity can be calculated using the resistivity of two phases by the follow equation:

$$\rho = (1-t)\rho_{\mathrm{G}} + t\rho_{\mathrm{GB}} \tag{7}$$

where the subscripts G and GB refer to the grain and grain boundary phase, respectively. The size fraction of the grain boundary phase is denoted as $t = t_{\mathrm{GB}}/t_{\mathrm{G}}$. By applying the series circuit model to our samples with two phases, α-MgAgSb and metallic Ag_3Sb, assuming ρ_{G} = 1 μΩ·m, ρ_{GB} = 0.1 Ω·m, and t_{GB} = 2 nm, we calculated the grain sizes to be 6 μm for sample S1, 7 μm for S2, 9 μm for S3, and 14 μm for S4. The variation in grain size calculated by this model aligns with estimates derived from the Williamson-Hall plot and SEM images. Consequently, the reduction in electrical resistivity is attributed to the increase in grain sizes, as depicted in Fig. S7. This demonstrates that the large grain size enhances electronic transport properties, leading to a higher power factor.

The Seebeck coefficients of the samples are nearly constant, except for sample S1. This is because the Seebeck coefficient is not influenced significantly by the carrier scattering rates. This tendency is clearly observed in comparisons between single crystal and polycrystalline of a sample material [59,66,67]. However, the Seebeck coefficient is generally proportional to the inverse of carrier concentration, consistent with our observation. Sample S4 exhibits the lowest electrical resistivity and a well-maintained Seebeck coefficient, as illustrated in Fig. 4(a) and (b). Consequently, the power factor of S4 has significantly improved, as depicted in Fig. 4(d). This demonstrates that the large grain size enhances electronic transport properties, leading to the higher power factor.

The total thermal conductivity consists of the summation of electronic and lattice thermal conductivity. The electronic thermal conductivity is given by $\kappa_{\mathrm{e}} = LT\sigma$, where L is the Lorenz number by Wiedemann-Franz's law. We calculated the Lorenz number to determine the electronic and lattice thermal conductivities using a single parabolic model [68]. The temperature-dependent Lorenz number and electronic thermal conductivity of the samples are illustrated in Fig. S8, with detailed equations provided in Supplementary Information (Supplementary note 2). The thermal conductivity of the samples decreases with the reduction of impurities and the increase of α-MgAgSb content within the materials, as shown in Fig. 5(a). Sample S1, which contains a large amount of impurity phases, exhibits high thermal conductivity. The increase in thermal conductivity implies the distinctive metallic properties of Ag_3Sb. Generally, metals have higher Debye temperatures compared to semiconductors due to stronger atomic bonds and faster vibrational frequencies. As listed in Table S8, the measured sound velocity and Debye temperature increase with higher Ag_3Sb content, reflecting the higher Debye temperature and faster sound velocity typically associated with metals compared to semiconductors. Since thermal conductivity is proportional to sound velocity, the increased sound velocity leads to an increase in lattice thermal conductivity. This correlation between higher sound velocity and increased thermal conductivity highlights the impact of the metallic nature of Ag_3Sb within α-MgAgSb.

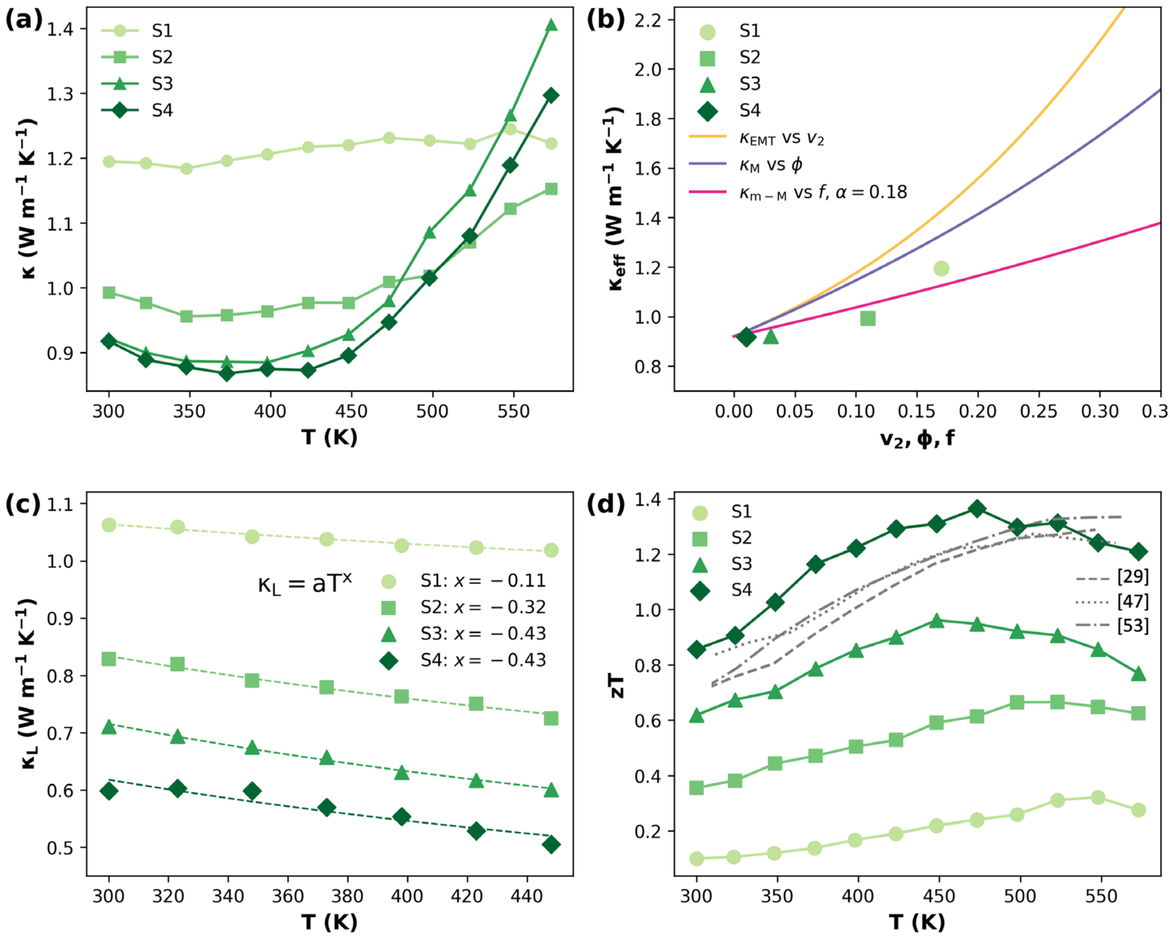

Fig. 5. (a) Temperature-dependent thermal conductivity of samples S1, S2, S3, and S4. (b) Effective thermal conductivity according to the EMT, Maxwell theory, and modified Maxwell theory (denoted m-M), alongside the thermal conductivity of samples S1, S2, S3, and S4. Temperature-dependent (c) lattice thermal conductivity, and (d) zT of samples S1, S2, S3, and S4 with literature values for $MgAg_{0.97}Sb_{0.99}$ synthesized by two-step BM (for 8 h and 5 h) [29], $MgAg_{0.97}Sb_{0.995}$ with an additional cleaning step of BM jar [47] and tantalum-sealed melted MgAgSb [53].

We conduct a quantitative investigation into the increase in thermal conductivity with increasing impurity levels using three methods: EMT, Maxwell theory and modified Maxwell theory, which describe the effective thermal conductivity of materials with multi-phases. Despite the presence of various impurity phases in samples S1 and S2, which contain significant quantities and types of impurities, our analysis primarily focused on Ag_3Sb due to its distinctive metallic properties compared to other phases. Among the impurities present in all four samples, Ag_3Sb exhibited the most systematic variation. We could disregard Sb due to its low quantity, and other phases like Mg_3Sb and γ-MgAgSb were excluded because of their semiconductor characteristics. This simplification allowed us to categorize the samples into two primary phases: α-MgAgSb and metallic Ag_3Sb.

Considering the intrinsically low thermal conductivity of α-MgAgSb (0.7–1.11 W m^{-1} K^{-1}) [39,52,69] and the significantly higher thermal conductivity of Ag_3Sb (6.26 W m^{-1} K^{-1}, as listed in Table S7), the thermal conductivity of the samples is expected to be influenced predominantly by the amount of Ag_3Sb present. This prediction is well-supported by the EMT. The effective thermal conductivity, κ_{eff}, by EMT can be calculated by the following equation [64,65]:

$$v_1 \frac{\kappa_1 - \kappa_{\text{eff}}}{\kappa_1 + 2\kappa_{\text{eff}}} + v_2 \frac{\kappa_2 - \kappa_{\text{eff}}}{\kappa_2 + 2\kappa_{\text{eff}}} = 0 \qquad (8)$$

where κ_1 and κ_2 are the thermal conductivity of phase 1 and phase 2, and v_1 and v_2 are the volume fractions of phase 1 and phase 2, respectively. However, as depicted in Fig. 5(b), the experimental thermal conductivity values at room temperature are lower than those predicted by EMT. This discrepancy suggests that while EMT provides a qualitative framework for understanding the thermal conductivity trends based on phase composition, additional factors such as microstructural features or interactions between phases may influence the actual thermal conductivity observed experimentally.

The Maxwell theory specifically addresses the effective thermal conductivity of materials containing dispersed spherical inclusions, while the EMT focuses on predicting averaged material properties. The effective thermal conductivity by Maxwell theory is calculated by [70]:

$$\kappa_{\mathrm{eff}} = \kappa_{\mathrm{m}} \frac{2\kappa_{\mathrm{m}}+\kappa_{\mathrm{p}}-2\phi(\kappa_{\mathrm{m}}-\kappa_{\mathrm{p}})}{2\kappa_{\mathrm{m}}+\kappa_{\mathrm{p}}+\phi(\kappa_{\mathrm{m}}-\kappa_{\mathrm{p}})} \tag{9}$$

Here, κ_{m} and κ_{p} denote the thermal conductivities of the matrix and spherical particles, respectively. ϕ represents the volume fraction of the particles. The effective thermal conductivity calculated from Maxwell theory decreases compared to EMT, as depicted in Fig. 5(b). However, Maxwell theory still cannot quantitatively describe the thermal conductivity of samples S1, S2, S3, and S4.

The modified Maxwell model integrates interfacial thermal barrier resistance for materials with spherical inclusions, addressing structural complexities that EMT and Maxwell theory may not fully account for. According to the modified Maxwell theory, the effective thermal conductivity of a multi-phase compound is expressed as [71]:

$$\kappa_{\mathrm{eff}} = \kappa_{\mathrm{m}} \frac{\kappa_{\mathrm{p}}(1+2\alpha)+2\kappa_{\mathrm{m}}+2f[(\kappa_{\mathrm{p}}(1-\alpha)-\kappa_{\mathrm{m}}]}{\kappa_{\mathrm{p}}(1+2\alpha)+2\kappa_{\mathrm{m}}-f[(\kappa_{\mathrm{p}}(1-\alpha)-\kappa_{\mathrm{m}}]} \tag{10}$$

Parameters α and f are dimensionless, where α is defined as a_{k}/a, indicating the ratio of the Kapitza radius (a_{k}=$R_{\mathrm{Bd}}\kappa_{\mathrm{m}}$) to the radius ($a$) of the dispersed particles, and f is the volume fraction of embedded particles. When $\alpha > 1$, the effective thermal conductivity becomes lower than the κ_{m}. Conversely, the κ_{eff} increases when the particle radius exceeds the Kapitza radius. This reflects that the size of spherical inclusions should be small in order to reduce the thermal conductivity, which is a key method for enhancing thermoelectric performance.

In SEM images (Figs. 2(c) and S3(a)), since the Ag_3Sb particles were several micrometers in size, a was set to 3 micrometers, resulting in a fitting parameter, α, of 0.18. As shown in Fig. 5(b), the increase in thermal conductivity with higher Ag_3Sb content in samples aligns well with the predictions from the modified Maxwell model. This model, which incorporates both interfacial resistance and particle shape, effectively explains the variation in thermal conductivity of samples S1, S2, S3, and S4. The thermal conductivity of samples S1, S2, S3, and S4 is influenced not only by the shape of dispersed particles but also by thermal boundary resistance. The distribution of Ag_3Sb within the α-MgAgSb matrix significantly enhances interfacial resistance, which emerges as a crucial factor.

At high temperatures ($T > \theta_{\mathrm{D}}$), the phonon–phonon (Umklapp) scattering predominates, described by the Debye-Callaway model with the relationship [72–74]:

$$\kappa_{\mathrm{L}} \approx \frac{k_{\mathrm{B}}^2\theta_{\mathrm{D}}}{2\pi^2 v_{\mathrm{s}} T} \propto \frac{1}{T} \tag{11}$$

Samples S1, S2, S3, and S4 exhibit a weak temperature dependence in lattice thermal conductivity, as depicted in Fig. 5(c). Unlike typical cases where $\kappa_{\mathrm{L}} \propto T^{-1}$ at high temperatures, the temperature exponent x values, $\kappa_{\mathrm{L}} \propto T^{x}$, of our samples are -0.11 for S1, -0.32 for S2, -0.43 for S3, and -0.43 for S4, respectively. The deviation from the $\kappa_{\mathrm{L}} \propto T^{-1}$ trend in α-MgAgSb was examined using theoretical phonon calculations [75]. The phonon scattering rate of α-MgAgSb shows minimal variation between 300 and 600 K, which indicates that phonon scattering is nearly independent of temperature. This observation gives rise to the weak temperature dependence of lattice thermal conductivity in samples S1, S2, S3, and S4, as the reduced temperature sensitivity of phonon scattering limits the expected κ_{L} decline typically observed at high temperatures.

As depicted in Fig. 5(d), the zT values of the samples are ranked in order of impurity content. Sample S1, with high impurity phase content and low carrier mobility, exhibited the lowest zT. In contrast, sample S4, characterized by an almost "impurity-free" α-MgAgSb compound (with only 1% antimony), showed the significantly enhanced zT across all temperature ranges. The peak zT value of 1.36 was achieved by sample S4 at 473 K.

4. Conclusion

In this study, our exploration of α-MgAgSb through varied ball milling techniques provides insights into crystal structure, microstructure, electronic, thermal transport properties, and thermoelectric performance. Systematic adjustment of BM conditions allowed us to control grain size, resulting in the enhancement of charge carrier mobility, the reduction of resistivity, and the improvement of thermoelectric performance of α-MgAgSb. The analysis of electrical resistivity and thermal conductivity contributes significantly to the understanding of how α-MgAgSb can be optimized for the enhancement of thermoelectric performance. α-MgAgSb with lower Sb content favors electron-electron scattering, while higher impurity levels introduce electron-phonon scattering, which diminishes carrier mobility. Additionally, thermal conductivity analysis comparing three different methods revealed that the distribution of Ag_3Sb significantly enhances interfacial resistance. These results underscore the importance of precise control over synthesis conditions to optimize the thermoelectric performance of α-MgAgSb. This study contributes to a deeper understanding of α-MgAgSb and provides a basis for further employing α-MgAgSb as thermoelectric materials.

Declaration of competing interest

The authors declare no conflict of interest.

Author contributions

Song Yi Back: Conceptualization, Investigation, Methodology, Formal analysis, Visualization, Writing-Original draft, **Steph Meikle**: Investigation, Methodology, Validation, Writing-Original draft, **Takao Mori:** Conceptualization, Writing-Reviewing and Editing, Supervision, Project administration, Funding acquisition

Acknowledgements

This work was financially supported by JST Mirai Program (No. JPMJMI19A1).

References

[1] L.E. Bell, Science 321 (2008) 1457–1461.
[2] H. Terry, T. Caillat, T. Mori, Energies 15 (2022) 7307.
[3] G. Min, Energy Environ. Sci. 15 (2022) 356–367.
[4] R. Chetty, J. Babu, T. Mori, Joule 8 (2024) 556–562.
[5] B. Poudel, Q. Hao, Y. Ma, Y. Lan, A. Minnich, B. Yu, X. Yan, D. Wang, A. Muto, D. Vashaee, X. Chen, J. Liu, M.S. Dresselhaus, G. Chen, Z. Ren, Science 320 (2008) 634–638.
[6] K. Biswas, J. He, I.D. Blum, C.-I. Wu, T.P. Hogan, D.N. Seidman, V.P. Dravid, M.G. Kanatzidis, Nature 489 (2012) 414–418.
[7] J. He, T.M. Tritt, Science 357 (2017) eaak9997.
[8] T. Mori, Small 13 (2017) 1702013.
[9] J. Mao, Z. Liu, J. Zhou, H. Zhu, Q. Zhang, G. Chen, Z. Ren, Adv. Phys. 67 (2018) 69–147.
[10] J.P. Heremans, V. Jovovic, E.S. Toberer, A. Saramat, K. Kurosaki, A. Charoenphakdee, S. Yamanaka, G.J. Snyder, Science 321 (2008) 554–557.
[11] Y. Pei, X. Shi, A. LaLonde, H. Wang, L. Chen, G.J. Snyder, Nature 473 (2011) 66–69.
[12] W. Liu, X. Tan, K. Yin, H. Liu, X. Tang, J. Shi, Q. Zhang, C. Uher, Phys. Rev. Lett. 108 (2012) 166601.
[13] Y.N. Yoshimasa Nishio, T.H. Tohru Hirano, Jpn. J. Appl. Phys. 36 (1997) 170–174.
[14] K. Kishimoto, T. Koyanagi, J. Appl. Phys. 92 (2002) 2544–2549.
[15] J.P. Heremans, C.M. Thrush, D.T. Morelli, Phys. Rev. B 70 (2004) 115334.
[16] K.F. Hsu, S. Loo, F. Guo, W. Chen, J.S. Dyck, C. Uher, T. Hogan, E.K. Polychroniadis, M.G. Kanatzidis, Science 303 (2004) 818–821.
[17] W. Kim, J. Zide, A. Gossard, D. Klenov, S. Stemmer, A. Shakouri, A. Majumdar, Phys. Rev. Lett. 96 (2006) 045901.
[18] M. Samanta, S. Roychowdhury, J. Ghatak, S. Perumal, K. Biswas, Chem. Eur. J. 23 (2017) 7438–7443.
[19] F. Kim, B. Kwon, Y. Eom, J.E. Lee, S. Park, S. Jo, S.H. Park, B.-S. Kim, H.J. Im, M.H. Lee, T.S. Min, K.T. Kim, H.G. Chae, W.P. King, J.S. Son, Nat. Energy 3 (2018) 301–309.

[20] I.T. Witting, F. Ricci, T.C. Chasapis, G. Hautier, G.J. Snyder, Research 2020 (2020) 4361703.

[21] Y. Lu, Y. Zhou, W. Wang, M. Hu, X. Huang, D. Mao, S. Huang, L. Xie, P. Lin, B. Jiang, B. Zhu, J. Feng, J. Shi, Q. Lou, Y. Huang, J. Yang, J. Li, G. Li, J. He, Nat. Nanotechnol. 18 (2023) 1281–1288.

[22] T. Mori, Nat. Nanotechnol. 18 (2023) 1255–1256.

[23] W.-D. Liu, L.-C. Yin, L. Li, Q. Yang, D.-Z. Wang, M. Li, X.-L. Shi, Q. Liu, Y. Bai, I. Gentle, L. Wang, Z.-G. Chen, Energy Environ. Sci. 16 (2023) 5123–5135.

[24] M.J. Kirkham, A.M. Dos Santos, C.J. Rawn, E. Lara-Curzio, J.W. Sharp, A.J. Thompson, Phys. Rev. B 85 (2012) 144120.

[25] J.-L. Mi, P.-J. Ying, M. Sist, H. Reardon, P. Zhang, T.-J. Zhu, X.-B. Zhao, B.B. Iversen, Chem. Mater. 29 (2017) 6378–6388.

[26] D. Li, H. Zhao, S. Li, B. Wei, J. Shuai, C. Shi, X. Xi, P. Sun, S. Meng, L. Gu, Z. Ren, X. Chen, Adv. Funct. Mater. 25 (2015) 6478–6488.

[27] X. Li, P.-F. Liu, E. Zhao, Z. Zhang, T. Guidi, M.D. Le, M. Avdeev, K. Ikeda, T. Otomo, M. Kofu, K. Nakajima, J. Chen, L. He, Y. Ren, X.-L. Wang, B.-T. Wang, Z. Ren, H. Zhao, F. Wang, Nat. Commun. 11 (2020) 942.

[28] P. Ying, X. Li, Y. Wang, J. Yang, C. Fu, W. Zhang, X. Zhao, T. Zhu, Adv. Funct. Mater. 27 (2017) 1604145.

[29] Z. Liu, Y. Wang, J. Mao, H. Geng, J. Shuai, Y. Wang, R. He, W. Cai, J. Sui, Z. Ren, Adv. Energy Mater. 6 (2016) 1502269.

[30] J. Mao, H. Zhu, Z. Ding, Z. Liu, G.A. Gamage, G. Chen, Z. Ren, Science 365 (2019) 495–498.

[31] Z. Liu, N. Sato, W. Gao, K. Yubuta, N. Kawamoto, M. Mitome, K. Kurashima, Y. Owada, K. Nagase, C.-H. Lee, J. Yi, K. Tsuchiya, T. Mori, Joule 5 (2021) 1196–1208.

[32] Z. Liu, W. Gao, H. Oshima, K. Nagase, C.-H. Lee, T. Mori, Nat. Commun. 13 (2022) 1120.

[33] P. Ying, L. Wilkens, H. Reith, N.P. Rodriguez, X. Hong, Q. Lu, C. Hess, K. Nielsch, R. He, Energy Environ. Sci. 15 (2022) 2557–2566.

[34] P. Ying, H. Reith, K. Nielsch, R. He, Small 18 (2022) 2201183.

[35] L. Wang, N. Sato, Y. Peng, R. Chetty, N. Kawamoto, D.H. Nguyen, T. Mori, Adv. Energy Mater. 13 (2023) 2301667.

[36] A. Li, Y. Wang, Y. Li, X. Yang, P. Nan, K. Liu, B. Ge, F. Chenguang, Z. Tiejun, Nat. Commun. 15 (2024) 5108.

[37] L. Wang, W. Zhang, S.Y. Back, N. Kawamoto, D.H. Nguyen, T. Mori, Nat. Commun. 15 (2024) 6800.

[38] H. Cho, S.Y. BACK, Naoki Sato, Z. Liu, W. Gao, L. Wang, H.D. Nguyen, N. Kawamoto, T. Mori, Adv. Funct. Mater. (2024) 2407017.

[39] X. Tan, L. Wang, H. Shao, S. Yue, J. Xu, G. Liu, H. Jiang, J. Jiang, Adv. Energy Mater. 7 (2017) 1700076.

[40] P. Ying, X. Liu, C. Fu, X. Yue, H. Xie, X. Zhao, W. Zhang, T. Zhu, Chem. Mater. 27 (2015) 909–913.

[41] T. Zhang, B. Dong, X. Wang, J. Mater. Sci. 56 (2021) 13715–13722.

[42] Y. Zheng, C. Liu, L. Miao, H. Lin, J. Gao, X. Wang, J. Chen, S. Wu, X. Li, H. Cai, RSC Adv. 8 (2018) 35353–35359.

[43] Y. Zheng, C. Liu, L. Miao, C. Li, R. Huang, J. Gao, X. Wang, J. Chen, Y. Zhou, E. Nishibori, Nano Energy 59 (2019) 311–320.

[44] Z. Liu, Y. Zhang, J. Mao, W. Gao, Y. Wang, J. Shuai, W. Cai, J. Sui, Z. Ren, Acta Mater. 128 (2017) 227–234.

[45] Z. Liu, J. Shuai, J. Mao, Y. Wang, Z. Wang, W. Cai, J. Sui, Z. Ren, Acta Mater. 102 (2016) 17–23.

[46] L. Xie, J. Yang, Z. Liu, N. Qu, X. Dong, J. Zhu, W. Shi, H. Wu, G. Peng, F. Guo, Y. Zhang, W. Cai, H. Wu, H. Zhu, H. Zhao, Z. Liu, J. Sui, Mater. Today 65 (2023) 5–13.

[47] A. Duparchy, L. Millerand, J. Camut, S. Tumminello, H. Kamila, R. Deshpande, A. Cowley, E. Mueller, J. De Boor, J. Mater. Chem. A 10 (2022) 21716–21726.

[48] Z. Liu, H. Geng, J. Mao, J. Shuai, R. He, C. Wang, W. Cai, J. Sui, Z. Ren, J. Mater. Chem. A 4 (2016) 16834–16840.

[49] Y. Liao, J.-L. Chen, C. Liu, J. Liang, Q. Zhou, P. Wang, L. Miao, J. Mater. Chem. C 10 (2022) 3360–3367.

[50] X. Zhang, H. Zhu, X. Dong, Z. Fan, Y. Yao, N. Chen, J. Yang, K. Guo, J. Hao, L. He, G. Li, H. Zhao, Joule 8 (2024) 3324-3335.

[51] J. Camut, I. Barber Rodriguez, H. Kamila, A. Cowley, R. Sottong, E. Mueller, J. De Boor, Materials 12 (2019) 1857.

[52] H. Zhao, J. Sui, Z. Tang, Y. Lan, Q. Jie, D. Kraemer, K. McEnaney, A. Guloy, G. Chen, Z. Ren, Nano Energy 7 (2014) 97–103.

[53] Y. Huang, J. Lei, H. Chen, Z. Zhou, H. Dong, S. Yang, H. Gao, T.-R. Wei, K. Zhao, X. Shi, Acta Mater. 249 (2023) 118847.

[54] S. Li, J. Yang, Y. Liu, J. Xin, S. Li, Q. Long, Q. Jiang, Adv. Appl. Ceram. 119 (2020) 107–113.

[55] M. Ladd, R. Palmer, Structure Determination by X-Ray Crystallography: Analysis by X-Rays and Neutrons, Springer US, Boston, MA, 2013.

[56] J. Sui, J. Shuai, Y. Lan, Y. Liu, R. He, D. Wang, Q. Jie, Z. Ren, Acta Mater. 87 (2015) 266–272.

[57] Z. Liu, Y. Wang, W. Gao, J. Mao, H. Geng, J. Shuai, W. Cai, J. Sui, Z. Ren, Nano Energy 31 (2017) 194–200.

[58] W. Gao, X. Yi, B. Cui, Z. Wang, J. Huang, J. Sui, Z. Liu, J. Mater. Chem. C 6 (2018) 9821–9827.

[59] G.J. Snyder, A.H. Snyder, M. Wood, R. Gurunathan, B.H. Snyder, C. Niu, Adv. Mater. 32 (2020) 2001537.

[60] J.M. Ziman, Electrons and Phonons: The Theory of Transport Phenomena in Solids, Reprinted, Clarendon Press, Oxford, 2007.

[61] S. Arrhenius, Zeitschrift für Physikalische Chemie 4 (1889) 226-248.

[62] N. Ashcroft, N.D. Mermin, Solid State Physics, Saunders College Publishing, 1976.

[63] C. Kittel, Introduction to Solid State Physics, 8th Edition, John Wiley and Sons, 2005.

[64] D.A.G. Bruggeman, Ann. Phys. 416 (1935) 636–664.

[65] D. Stroud, Phys. Rev. B 12 (1975) 3368–3373.

[66] J.J. Kuo, S.D. Kang, K. Imasato, H. Tamaki, S. Ohno, T. Kanno, G.J. Snyder, Energy Environ. Sci. 11 (2018) 429–434.

[67] M.T. Dylla, J.J. Kuo, I. Witting, G.J. Snyder, Adv. Mater. Interfaces 6 (2019) 1900222.

[68] H.-S. Kim, Z.M. Gibbs, Y. Tang, H. Wang, G.J. Snyder, APL Mater. 3 (2015) 041506.

[69] C.Y. Sheng, H.J. Liu, D.D. Fan, L. Cheng, J. Zhang, J. Wei, J.H. Liang, P.H. Jiang, J. Shi, J. Appl. Phys. 119 (2016) 195101.

[70] J.C. Maxwell, A Treatise on Electricity and Magnetism, Cambridge University Press, 1873.

[71] A.G. Every, Y. Tzou, D.P.H. Hasselman, R. Raj, Acta Mater. 40 (1992) 123–129.

[72] P. Debye, Ann. Phys. 344 (1912) 789–839.

[73] J. Callaway, Phys. Rev. 113 (1959) 1046–1051.

[74] E.S. Toberer, A. Zevalkink, G.J. Snyder, J. Mater. Chem. 21 (2011) 15843.

[75] Z. Zhang, Y. Zhu, J. Ji, J. Zhang, H. Luo, C. Fu, Q. Li, M. Brod, G.J. Snyder, Y. Zhang, J. Yang, W. Zhang, Mater. Today Phys. 25 (2022) 100702.